

# Spectral effects on the energy harvesting efficiency of 2- and 4-terminal tandem photovoltaics

Robert Witteck<sup>\*1</sup>, John. F. Geisz<sup>1</sup>, Emily. L. Warren<sup>1</sup>, and William. E. McMahon<sup>1</sup>

<sup>1</sup>National Renewable Energy Laboratory, Golden, CO, USA

September 28, 2023

## Abstract

In this work, we investigate how a varying spectral irradiance and top cell bandgap affect the energy yield of 2-terminal (2T) and 4-terminal (4T) perovskite//silicon tandem solar cells under outdoor operating conditions. For the comparison, we first validate an optoelectronic model employing a 1-year outdoor data set for a 4T mechanical stacked gallium arsenide (GaAs) on crystalline silicon (Si) tandem device. We then use our verified model to simulate perovskite//silicon tandem devices with a varying perovskite top cell bandgap for a location in Golden, Colorado, USA. We introduce a spectral binning method to efficiently reduce and improve the visualization of the 1-min-resolved environmental data while maintaining the simulation accuracy. Our findings reveal that, for a device that is current-matched under standard testing conditions, the annual spectral deviation reduces the energy harvesting efficiency by only 2%<sub>rel</sub>. When additional realistic losses for the 4T are taken into account, 2T devices are shown to have an energy-harvesting efficiency that is at parity or higher. Deviations in the top cell bandgap of more than 0.1 eV from current matching result in a reduced energy-harvesting efficiency of more than 5%<sub>rel</sub> for the 2T tandem device.

## 1 Introduction

Modeling of energy-harvesting efficiency (EHE) can be used to assess the relative merits of various tandem cell architectures when operated under outdoor conditions [1]. Given the different spectral dependencies of tandem cells compared to single-junction solar cells, it is crucial to quantify their energy production under varying irradiance spectra. Here, we compare the simulated performance of 2-terminal (2T) and 4-terminal (4T) perovskite//silicon tandem cells over the course of a year in Golden, Colorado (USA). Many works have already shown that 2T devices may suffer from spectral mismatch losses [2, 3, 4, 5]. In 4T devices, the top and bottom cells can operate electrically independent, each at its own maximum power point (MPP). Thus, an idealized 4T device can serve as theoretical upper-limit benchmark in terms of annual energy yield performance. Consistent with the results of prior work, we find that 2T devices suffer from spectral mismatch losses. However, our results show that if the top and bottom cells are current-matched, these losses are only 2%<sub>rel</sub> when compared to an ideal 4T.

Our results include the anomalous temperature dependence for the bandgap of a perovskite solar cell (PSC), which can cause the external quantum efficiency ( $Q_c$ ) and the short-circuit current density ( $J_{sc}$ ) of a PSC to differ from those observed in traditional crystalline silicon (Si) solar cells [6]. This can affect which sub-cell is current-limiting as the temperature changes [7]. In turn, this impacts the spectral sensitivity of 2T cells and thereby their EHE. Hence, it is reasonable to anticipate deviations in our EHE findings for a PSC//Si tandem compared to tandems exhibiting more conventional temperature dependencies. However, our results are quantitatively similar to prior results for more traditional tandems.

Reynolds et al. [8] showed that, for micromorph Si 2T tandems, the efficiency loss for varying spectra is only 2%<sub>rel</sub> compared to that of a constant spectrum, assuming the 2T device is matched to the peak of the long-term energy distribution of the varying spectra. Futscher et al. [9] simulated an average efficiency for ideal 2T and 4T PSC//Si tandems, resulting in an annual efficiency advantage of 1.8%<sub>rel</sub> for the 4T device for a location in Golden, Colorado. They also showed that the efficiency of a tandem cells exceeds the efficiency of a single-junction Si cell for varying incident spectra. In contrast, we simulate the EHE of perovskite//silicon tandems based on experimentally determined sub-cell parameters and for a minutely measured spectrum in this work.

When evaluating the performance of different tandem architectures, it is common to use an idealized 4T device as a theoretical upper-limit benchmark. However, there is an inherent design compromise for actual 4T cells. This is because the contact layer between the top cell and the bottom cell must fulfill two roles: (i) it must be highly conductive to allow

---

<sup>\*</sup>Corresponding author: robert.witteck@nrel.gov

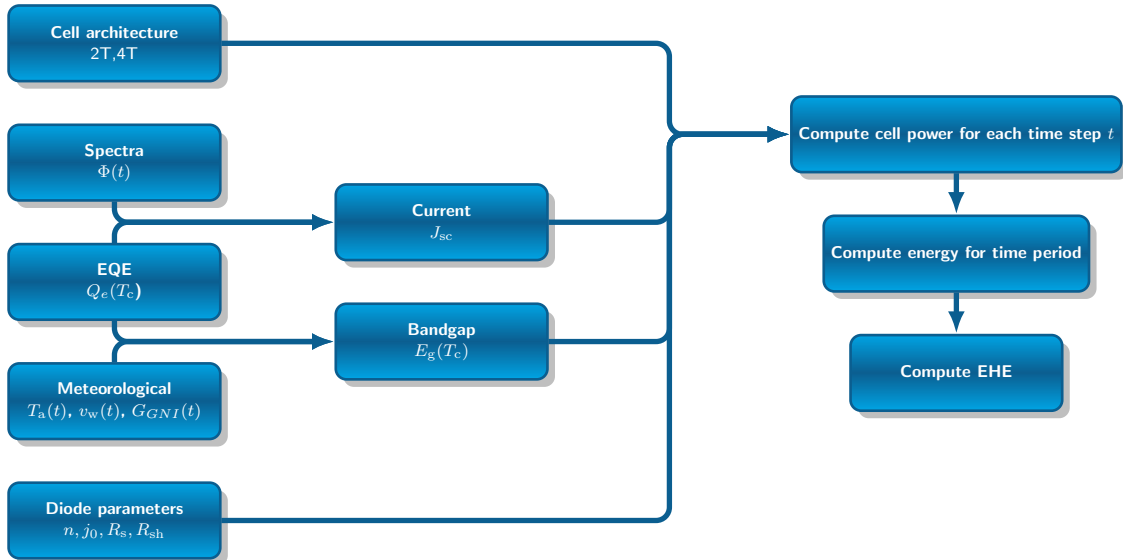


Figure 1: Modeling flow for the energy harvesting efficiency (EHE). The cell temperature  $T_c$  inside the module is derived from the ambient temperature  $T_a$ , wind speed  $v_w$ , and the global normal irradiance  $G_{GNI}$ , according to King et al. [11].

for lateral current transport to the terminals, and (ii) it must be highly transparent for photons that will be absorbed in the bottom cell. Thus, a careful EHE analysis must consider the different optical and resistive losses that might vary with the module architecture. For instance, a monolithic series interconnection for an all-perovskite (PSK) tandem has different optical and resistive losses than direct deposition or stacking of a PSK top cell onto an Si bottom cell. Langenhorst et al. [10] showed in a simulation study that, for a current-matched PSK//copper indium gallium diselenide (CIGS) tandem cell, the difference in energy yield between 2T and 4T devices is marginal. However, their results show that if the current-matching is poor, e.g., by using a PSK top cell with a bandgap of 1.55 eV, the 4T device will outperform the 2T device by 3.5 %.

In this work, we calculate and compare the EHE of 2T and 4T PSK//Si tandem cells for varying environmental and spectral conditions of a site in Golden, Colorado. We base our modeling on measured device parameters for PSC top cells with varying bandgaps on an Si bottom cell. The environmental and spectral data covers a full year with a 1-min resolution. This enables a comprehensive temporal energy yield comparison between 2T and 4T devices, accounting for spectral and temperature effects on the sub-cell performance. We present a spectral binning method to reduce the computational effort for this comparison, which allows a fast EHE comparison for different sites with varying spectral and environmental conditions. Besides computational benefits, the spectral binning also improves the visualization and makes differences between 2T and 4T harvesting efficiency more apparent.

## 2 Modeling flow

We simulate the EHE of different tandem cell architectures for a site in Golden, Colorado. Figure 1 shows our modeling flow to simulate the EHE. The central element is *PVcircuit*, an equivalent circuit-solver that facilitates the simulation of tandem solar cells with different architectures, while taking into account luminescent coupling [12]. *PVcircuit* requires the spectral data, meteorological data, temperature-dependent  $Q_c$ , cell architectures, and diode parameters to simulate the EHE. From the temperature-dependent  $Q_c$ , we obtain the temperature-dependent bandgap and  $J_{sc}$  of the sub-cells. We use the model from King et al. [11] to derive the cell temperature inside the photovoltaic (PV) module from the meteorological data, i.e., from the ambient temperature, wind speed, and irradiance. We extract the diode parameters from the individual sub-cell current density-voltage ( $J(V)$ ) measurements. *PVcircuit* then simulates the power output for each time step to determine the energy yield of the cell architecture and the EHE.

### 2.1 Solar cell parameters

We fabricate six PSCs with varying stoichiometry and measure their  $J(V)$  characteristics, transmittance, and  $Q_c$ . Detailed information on the cell processing procedures is available in Tong et al. [13] and Kim et al. [14]. The stoichiometric variation results in PSKs with varying bandgaps  $E_{g,25}$  of (1.58, 1.63, 1.68, 1.7, 1.75 and 1.8) eV, as determined from  $Q_c$  measurements at 25 °C [15]. A single-diode model (SDM) is used to extract the diode parameters from the measured  $J(V)$  characteristics. These PSCs serve as potential top cells. For the Si bottom cell, we measure the  $J(V)$  characteristics

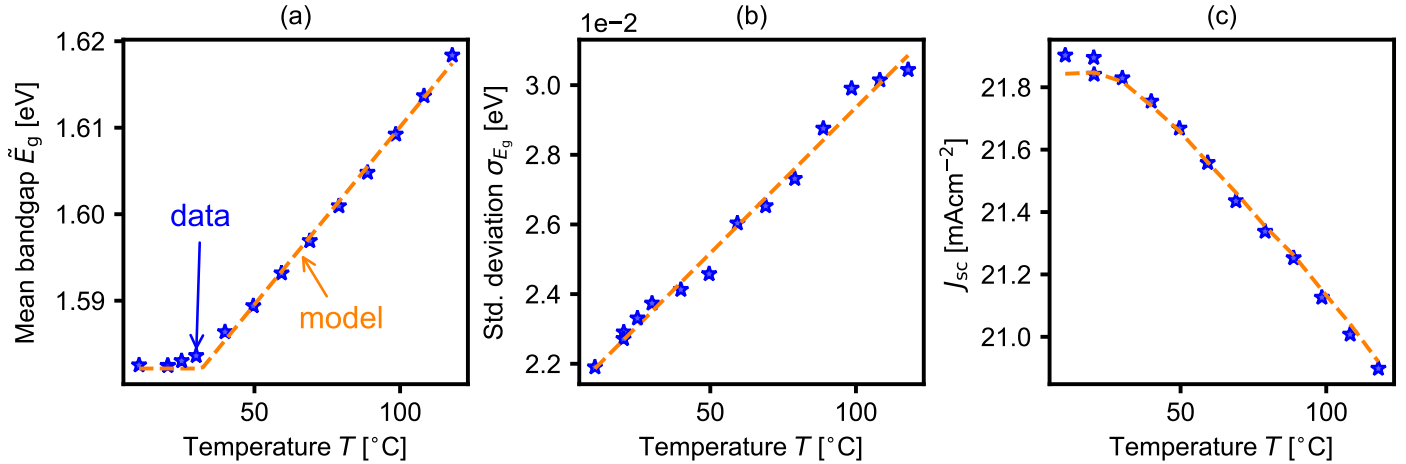


Figure 2: Temperature dependence of  $\tilde{E}_g$  and  $\sigma_{E_g}$  for the PSC. Blue symbols indicate measurements and dashed lines modeling according to Equations 1 employing the parameters in Table 1.

Table 1: Temperature coefficients for  $\tilde{E}_g$  and  $\sigma_{E_g}$

Cell	$\alpha$ [eV °C <sup>-1</sup> ]	$\beta$ [eV]	$a$ [eV °C <sup>-1</sup> ]	$b$ [eV]
PSC <sup>a</sup>	$4.11 \times 10^{-4}$	1.57	$8.36 \times 10^{-5}$	$2.10 \times 10^{-2}$
Si	$-6.27 \times 10^{-4}$	1.17	$2.76 \times 10^{-4}$	$5.86 \times 10^{-2}$

<sup>a</sup>  $\tilde{E}_g(\alpha, \beta)$  if  $T > 32$  °C and 1.58 eV otherwise.

and  $Q_c$  of an poly-Si on oxide interdigitated back contact (POLO-IBC) Si cell and similarly fit the  $J(V)$  data with the SDM. We integrate the AM1.5G convolved  $Q_c$  to determine the  $J_{sc}$  of the bottom cell in a tandem solar cell, accounting for optical transmission through the various top cells. Using a PSK top cell with a bandgap of 1.70 eV results in a current-matched 2T PSK//Si tandem device for our experimental data.

## 2.2 Bandgap extraction and bandgap temperature dependence

We measure the temperature-dependent  $Q_c$  of the Si as well as the PSK solar cell with the bandgap of 1.58 eV and extract the bandgap for each temperature similar to the method of Rau et al. [15]. We fit the first derivative of the  $Q_c$  with a Gaussian function and extract the mean bandgap  $\tilde{E}_g$  and the standard deviation  $\sigma_{E_g}$ . Figure 2 (a) shows  $\tilde{E}_g$ , and Figure 2 (b) shows  $\sigma_{E_g}$  for the PSC. For the temperature dependence of  $\tilde{E}_g$  of the PSC, we assume a piecewise linear function, with a constant bandgap for temperatures below 32 °C and a linearly increasing bandgap for higher temperatures. This is in agreement with other bandgap temperature dependencies reported in the literature [6, 16]. For  $\sigma_{E_g}$  of the PSC as well as the  $\tilde{E}_g$  and  $\sigma_{E_g}$  for the Si cell, we assume a linear dependence for all temperatures

$$\tilde{E}_g = \alpha T + \beta \qquad \sigma_{E_g} = aT + b, \qquad (1)$$

where  $T$  is the temperature and  $\alpha$ ,  $\beta$ ,  $a$ , and  $b$  are material-specific coefficients, as summarized in Table 1.

Employing Equation 1 with the parameters in Table 1, we can determine  $\tilde{E}_g$  and  $\sigma_{E_g}$  for a given temperature and derive the corresponding  $Q_c$ . Figure 2 (c) demonstrates the applications of this approach for the PSC. The symbols indicate the  $J_{sc}$  extracted from the measured  $J(V)$  data, and the dashed line indicates the  $J_{sc}$  resulting from the integration of the AM1.5G convoluted and temperature-corrected  $Q_c$ . The advantage of using the  $Q_c$  to determine the  $J_{sc}$  is that, besides considering the temperature dependence, it also accounts for the mutual influence of top cell and bottom cell  $Q_c$ . In the energy yield modeling, we assume that this temperature dependence is the same for all PSCs of varying bandgaps.

## 2.3 Diode model

We model the output voltage  $V_{cell}$  and current density  $J_{cell}$  of the individual top and bottom solar cells using PVcircuit [17, 18]. PVcircuit employs a diode model with

$$V_{cell} = V_{diode} - JR_s$$

where  $c$  is the speed of light.

We obtain  $A_j$ ,  $n_{0j}$ , and  $J_{sc}$  from fitting the diode equation to  $J(V)$  measurements of individual solar cells at standard testing conditions (STC). PVcircuit also accounts for luminescent coupling between the sub-cells. Here, we follow the approach of Geisz et al. [17], employing a  $\beta$  of 16 for the bottom cell.

## 2.4 Meteorological data

We use the environmental data measured at the NREL Solar Radiation Research Laboratory (SRRL) in Golden, Colorado, to simulate the energy yield of the tandem devices [20]. The data set spans a period of one year (November 1, 2021 until October 31, 2022) and has a 1-min resolution. For the spectral data, we use the measurements from the two-axis tracked EKO Instruments WISER MS-712 spectroradiometer, denoted  $\Phi_{\text{GNI}}$ . We calculate the resulting global normal irradiance (GNI) as

$$G_{\text{GNI}} = \int_{290}^{1650} \Phi_{\text{GNI}} d\lambda,$$

where  $\lambda$  is the wavelength.

To derive the cell temperature inside the module, we employ the model from King et al. [11], which takes the irradiance, wind speed, and ambient temperature into account. Data affected by instrument maintenance schedules and spectra with negative values are discarded.

## 2.5 Model verification

We compare the power output simulated with PVcircuit to the measured power output of a GaAs//Si 4T tandem solar module [21] to verify our model. The module was monitored for one year at the location in Golden, Colorado. We chose a gallium arsenide (GaAs)-on-Si 4T tandem cell for the model verification because both materials are more resilient to outdoor degradation and operate more stable than e.g., PSK [22, 23]. Hence, the associated cell parameters needed for numerical modeling did not change significantly over the course of the year. A current-voltage ( $I(V)$ ) curve tracer measures the  $I(V)$  characteristics of the top and bottom cell every 2 min. For further details on the tandem module and the measurements, we refer to Springer et al. [24].

Following the model flow in Figure 1, we simulate the module power of the tandem device using measured site spectra and meteorological data. Figure 3(a) shows an identity plot comparing the measured and simulated module power. The orange dashed line is the identity line (where the measured module power is equal to the simulated module power). The majority of the data points align along this identity line. We use the Pearson correlation coefficient  $R$  to quantify the correlation between measurement and simulation. For the data in Figure 3(a), we obtain an  $R$ -value of 0.9697, where an  $R$ -value of 1.0 means an exact match of measurement and simulation. This excellent agreement demonstrates the ability of PVcircuit to model the outdoor data with sufficient accuracy.

The variations between the measured and simulated module power stem primarily from discrepancies in the  $J_{sc}$  values. Figure 3(b) shows the measured and simulated module power when using the measured  $J_{sc}$ , instead of the  $J_{sc}$  from integrated  $Q_c$  convoluted spectra, as input parameters for PVcircuit. This reduces the number of data points deviating from the identity line and improves the  $R$ -value to 0.9993. We ascribe the differences in  $J_{sc}$  to the different locations of the spectroradiometer and the solar module test site, as well as asynchronous measurement times. In addition, the measured  $J_{sc}$  accounts for a small degradation that we have observed over the year (see [24]), which is neglected in the  $J_{sc}$  determined from the integrated  $Q_c$ .

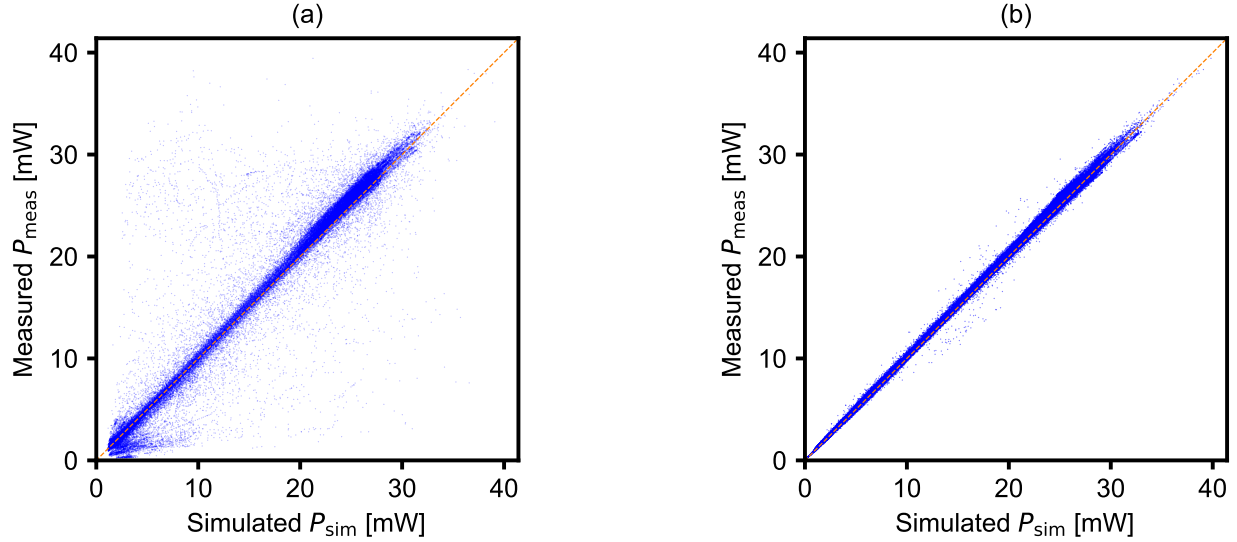


Figure 3: Measured vs. simulated module power for the 4T GaAs//Si tandem when (a) the  $J_{sc}$  from the integrated  $Q_c$  convoluted spectra is used as an input parameter for PVcircuit and (b) the measured current is used as input parameters.

## 2.6 Energy harvesting efficiency of PSC//Si tandems

After verifying PVcircuit for energy yield modeling, we use the environmental data from Section 2.4 to model the annual energy output  $E_{out}$  of a 2T and a 4T PSC//Si tandem solar module. The annual energy produced by the solar module is calculated as

$$E_{out} = \sum_t P_{out} t,$$

where  $P_{out}$  is the module power output for each time step  $t$ . The EHE allows us to quantify the efficiency of energy harvesting by considering the temporal and spectral aspects of the solar module's performance, and it relates the produced annual energy to the incident solar energy  $E_{GNI}$  as follows

$$\eta_{ehe} = \frac{E_{out}}{E_{GNI}} = \frac{E_{out}}{\sum_t E_{GNI,t}} = \frac{\sum_t P_{out} t}{\sum_t G_{GNI} t}. \quad (2)$$

## 3 Energy yield simulations

### 3.1 Spectral binning

Simulating the EHE for the full year using 1-min time intervals is computationally expensive. Thus, we reduce the amount of data by employing a spectral binning method that bins the spectra into sets of similar spectra. Each bin of spectra can then be represented with a single "proxy" spectrum. The method follows the approach presented by Garcia et al. [3], but instead of the equivalent photocurrent ratio, we use the APE. The APE of a solar spectrum is given by [25]

$$E_{ape} = \frac{hc}{q} \frac{\int \Phi_{GNI} d\lambda}{\int \Phi_{GNI} \lambda d\lambda},$$

where  $h$  is Planck's constant.

We assign each spectrum an APE and incident energy

$$E_{GNI} = G_{GNI} t.$$

Subsequently, we sort the spectra according to their APEs and calculate the cumulative sum of the energy for all spectra. We divide the maximum of the cumulative sum into  $N_{Sbins}$  equal energy bins. Figure 4(a) shows this for 10 bins. The orange dashed lines indicate the bin edges segmenting the cumulative sum of the energy, thus conserving the energy for each bin.

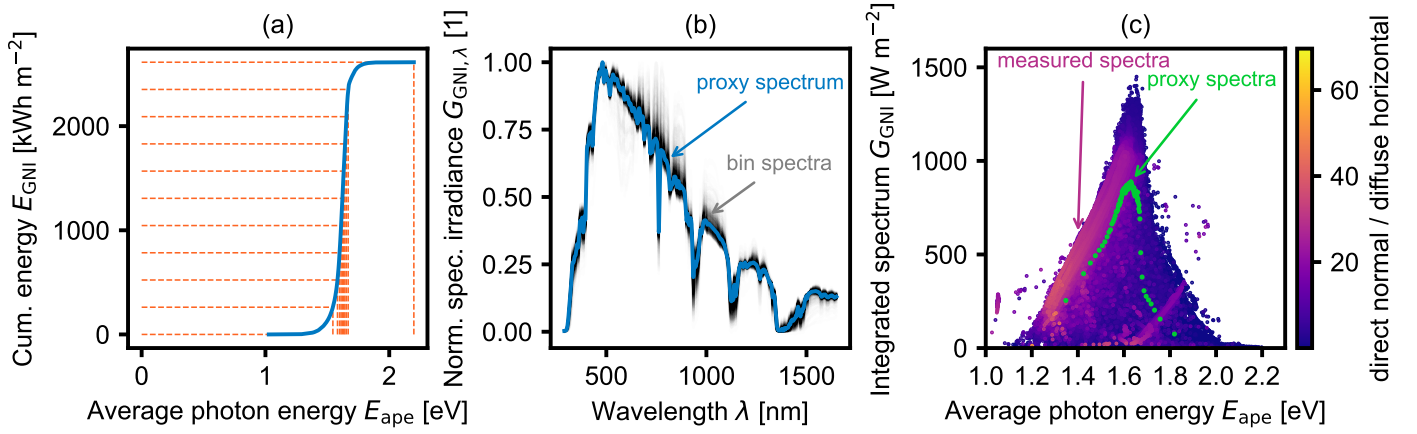


Figure 4: (a) Spectral binning by equal energy into 10 bins. The orange dashed lines show the bin edges, and the blue line shows the corresponding  $E_{GNI,k}$ . (b) The resulting proxy spectra of the fifth bin with a mean average photon energy (APE) of 1.63 eV, shown in blue. The underlying gray lines show every 20<sup>th</sup> spectrum in the bin. (c) The integrated irradiance for all spectra, colored by the direct-to-diffuse irradiance ratio. The superimposed green dots indicate the integrated irradiance of 100 proxy spectra.

The  $k^{\text{th}}$  bin out of the  $k = 1 \dots N_{Sbins}$  bins contains  $n_k$  spectra. We assign each of the  $l = 1 \dots n_k$  spectra  $\Phi_{kl}$  in a bin a time  $t_{kl}$  and temperature  $T_{kl}$ . Thus, the total time for each bin  $t_k$  is given as

$$t_k = \sum_{l=1}^{n_k} t_{kl}.$$

We can then assign each bin an average proxy spectrum by taking the mean of all spectra in this bin

$$\Phi_k^p = \frac{1}{t_k} \sum_{l=1}^{n_k} \Phi_{kl} t_{kl}.$$

Figure 4(b) illustrates this for the proxy spectra of the fifth bin in blue, with a mean APE of 1.64 eV. The underlying gray lines show every 20<sup>th</sup> spectrum in the bin. The original spectra are plotted in grey with some transparency, so overlapping spectra become darker in the graph. It is important to note that the proxy spectrum in blue represents the mean of all gray spectra, since the mean mathematically conserves the energy.

Figure 4(c) shows the integrated irradiance for all spectra colored by the direct/diffuse irradiance ratio. The integrated irradiance of the 100 proxy spectra is indicated by the superimposed green dots. The direct/diffuse ratio reveals that clear sky days with a high fraction of direct light are "red-rich" and have a lower APE. More diffuse light is "blue-rich" due to scattering of short wavelength photons by clouds, and has a higher APE. However, for the blue-shifted tail of the distribution, the higher cloud coverage also significantly reduces the irradiance. Consequently, these spectra provide light with shorter wavelengths but less incident energy over the course of the year. As a result, 90% of the energy of all spectra are in the range between 1.50 eV to 1.70 eV, consistent with Figure 4(a). Besides reducing the computational effort, the binning also helps visualize the relevant spectra that have the biggest impact on the energy yield.

In addition to the irradiance, the cell temperature inside the module is crucial for the outdoor performance of the tandem. We bin the temperatures of each spectral bin, denoted as  $T_{kl}$ , into  $N_{Tbins}$  cell temperature bins with equal bin width  $\Delta T$ . We then simulate the power output for each of the  $N_{Tbins}$  temperature bins for a given proxy spectra to calculate the EHE for this spectral bin as

$$\eta_{\text{ehe},k} = \frac{\sum_{m=1}^{N_{Tbins}} P_{\text{out},km} t_{km}}{\int \Phi_k^p d\lambda t_k}. \quad (3)$$

For each temperature bin, we employ its median temperature value. The EHE for all proxy spectra is then given by

$$\eta_{\text{ehe}} = \frac{\sum_{k=1}^{N_{Sbins}} \sum_{m=1}^{N_{Tbins}} P_{\text{out},km} t_{km}}{\sum_{k=1}^{N_{Sbins}} \int \Phi_k^p d\lambda t_k}.$$

With an increasing number of spectral and temperature bins, this will approximate the expression in Equation 2.

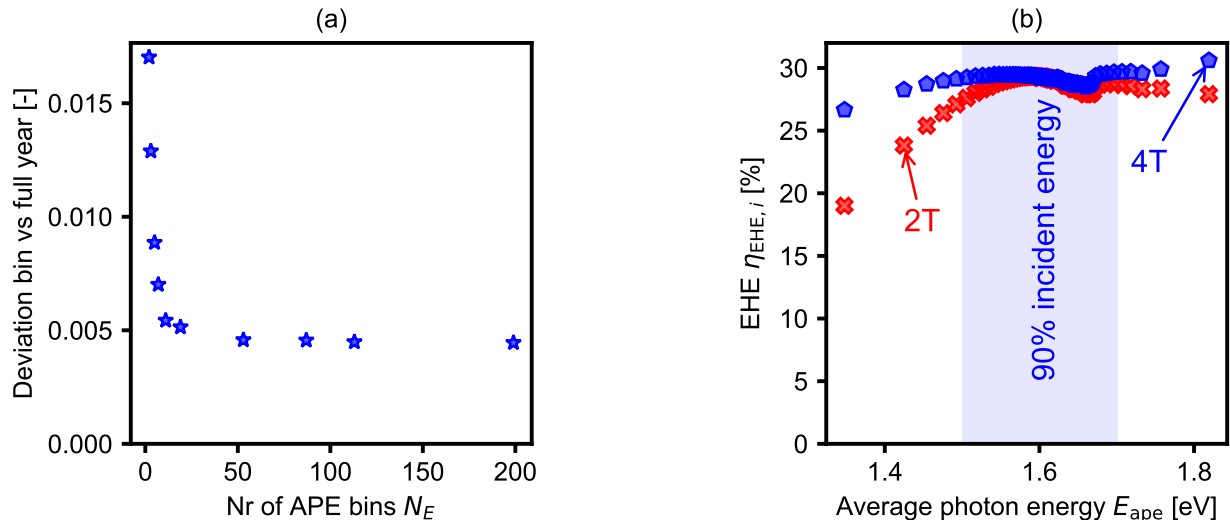


Figure 5: (a) Deviation in energy yield for the 2T device, when comparing the full-year energy yield with the equal energy binning approach using five temperature bins per spectral bin. (b) Comparison of the energy-harvesting efficiency for 2T and 4T devices for 100 proxy spectra. The blue area highlights the range that accounts for 90% of the energy of all incident spectra.

### 3.2 Comparing spectral binning and full-year EHE simulations

We compare the equal energy binning approach with full-year simulations by simulating a 2T and a 4T device. For a fair comparison between 2T and 4T devices, we choose a PSK top cell with a bandgap of 1.70 eV, as this results in a current-matched device for STC measurements with AM1.5G spectrum. For the full-year simulation, we simulate the power output of the 2T tandem device for each time step and calculate the annual energy yield. For the binning approach, we vary the number of bins  $N_{Sbins}$ , simulate the power output of the 2T tandem device, and calculate the annual energy yield considering the total time of each bin.

Figure 5 (a) shows the deviation in energy yield for the 2T device when comparing the full-year energy yield simulation with the binning approach. For each of the  $N_{Sbins}$  variations, we use five temperature bins. Employing more than 50 bins reduces the deviation between the full-year and binning approach to less than 0.5%. This is consistent with other methods of agglomerating spectral data using other binning methods [3] or machine learning methods [26]. Hence, this approach allows for a significant reduction in computational effort when comparing the EHE for different top-cell bandgaps combined with an Si bottom cell in 2T and 4T devices, while still ensuring accurate simulation results. For instance, on a conventional laptop, a full-year simulation takes several days, while a 50-bin simulation takes only a few minutes.

### 3.3 Comparing the EHE of 2T and 4T tandem cells

In this section, we compute the EHE for tandem cells comprising of a 1.70-eV PSC top cell and an Si bottom cell over the course of one year in Golden, Colorado. We choose the top cell with a bandgap of 1.70 eV, as this results in a current-matched tandem under the AM1.5G spectrum when employing an Si bottom cell. This enables a comparison of 2T and 4T cells, where both operate close to their optimum. We initially neglected resistive and optical losses to focus on losses due to spectral variation. These will be reintroduced later for a more complete comparison.

As described in the previous section, we use a spectral-binning algorithm to reduce the full set of spectra to a much smaller set in which proxy spectra represent sets of spectra with similar APE values. The cell power and EHE are computed for each proxy spectrum, as well as for the entire year, by considering the time for each bin.

Figure 5 (b) shows the computed efficiencies for 100 proxy spectra according to Equation 3. The APEs of the proxy spectra range from 1.35 eV to 1.82 eV. The 2T device is nearly current-matched for a spectra with an APE of 1.60 eV, so for spectra near this energy, the 2T and 4T efficiencies are nearly identical. Consequently, both sub-cells operate in close proximity to their respective MPPs. As the incident proxy spectra become more red- or blue-rich, the 2T efficiency becomes lower, because the sub-cells are no longer current-matched. However, 90% of the incident energy is provided by spectra with APE values between 1.50 eV and 1.70 eV (shaded blue region). In this region, the 2T efficiency is close to the 4T efficiency. As a result, the annual EHE of the 2T device is only 2%<sub>rel</sub> lower than the EHE of the 4T device. This result serves as the baseline for comparison in Table 2, where various scenarios of 4T-related optical and resistive

Table 2: Considered electrical and optical losses when integrating a 4T into a solar module.

Scenario	Rs [ $\Omega \text{ cm}^2$ ]	TCO loss 4T [%]	2T/4T energy yield [%]
1	0	0	98
2	1.86	0	100
3	0	5	100

losses are examined. The upshot is that despite encountering spectral variations during outdoor operation, the EHE of an STC current-matched 2T is only slightly smaller than that of a 4T device. This is consistent with the results for more traditional tandems [8], regardless of the anomalous temperature behavior of the PSC. One possible explanation is that operating the cell at the MPP makes the spectral and temperature effects marginal due to fill factor (FF) compensation [27, 28, 8, 29].

Furthermore, the architectural differences between 2T and 4T devices generally lead to distinct optical and resistive losses. The most significant difference is that a 2T device typically employs a thin tunnel or recombination junction in between the sub-cells, which creates low optical and resistive losses [30, 31]. In contrast, a 4T device requires an additional transport layer to facilitate lateral current transport between the sub-cells. Typically, this is accomplished by implementing a transparent conductive oxide (TCO) layer between the sub-cells. Thus, there is a trade-off between optical and resistive losses associated with this TCO layer. Assuming the TCO layer contributes an additional series resistance of  $1.87 \Omega \text{ cm}^2$  results in parity in the annual EHE between 2T and 4T devices. Similarly, optical losses of 5% for the bottom cell current, due to free carrier absorption in the TCO layer, would equalize the energy yield. Table 2 summarizes the results for both assumptions. Exceeding any of these inherent and unavoidable losses in the 4T device will result in the 2T device having a greater EHE than the 4T device.

Usually, both losses are intertwined and occur simultaneously. As an example, for our TCO with a sheet resistance of  $24 \Omega/\square$ , we obtain an additional series resistance contribution of  $1.82 \Omega \text{ cm}^2$  and optical losses of 2.2% for the bottom cell, which results in a higher EHE for the 2T device than for the 4T device. The exact losses will be situational and unique to specific devices. However, it can be beneficial to initially conduct a comparison with optical and resistive losses neglected, as this establishes a baseline for comprehending the significance of the different losses involved.

Given that current-matching is crucial for achieving peak 2T device performance, the choice of sub-cell bandgaps significantly impacts the 2T versus 4T EHE comparison. Figure 6 shows the simulated annual EHE for a 1-year operation in Golden. We simulate tandem cells with varying bandgaps for the PSK top cell featuring an Si bottom cell. In the calculations, we assume no additional resistive or optical losses for the 4T device, resulting in the previously mentioned EHE advantage of 2% for the current-matched device with a 1.70-eV bandgap for the top cell. Considering a non-optimal bandgap for the top cell of 1.58 eV results in a 17%<sub>rel</sub> lower annual EHE for the 2T device due to the higher current mismatch. Such high losses will be challenging to compensate for, even when considering additional losses due to the TCO layer which is necessary for the module integration of the 4T device. Hence, it is imperative to consider a well-current-matched device for the 2T tandem. Small variations in the bandgap of 0.05 eV only have a marginal impact on the annual EHE. However, it is important to acknowledge that wide-bandgap materials may exhibit additional challenges that can adversely impact the properties of the sub-cells [32, 33, 34].

Finally, the test site location in Golden has an average APE of 1.61 eV, which is close to the APE of 1.62 eV of the AM1.5G spectrum in the same wavelength range. Thus, the ideal combination of top cell and bottom cell bandgaps for a current-matched device may be different for locations that vary significantly from this value.

## 4 Summary and outlook

In this work, we provide a framework to perform energy yield simulations for 2T and 4T tandem solar cells considering varying outdoor spectra and top cell bandgaps. We verify our model by comparing the measured and simulated power output of a GaAs//Si tandem that was deployed outdoors for one year. Employing the measured device current as input parameters results in an excellent agreement between measurement and simulation, with a Pearson correlation coefficient of 0.9993.

We introduce a new spectral binning method that uses the average photon energy to agglomerate the spectral data. Besides reducing the computational effort, the binning approach also improves the data visualization to provide a better understanding of spectral effects on the tandem performance. Varying the number of bins and comparing it to the full-year simulation, we find that employing more than 50 bins reduces the deviation between full-year and binning approach to less than 0.5%. Thus, the binning method significantly reduces the computational effort for energy yield simulations while providing sufficient accuracy to compare the energy yield of different tandem architectures. One advantage of using



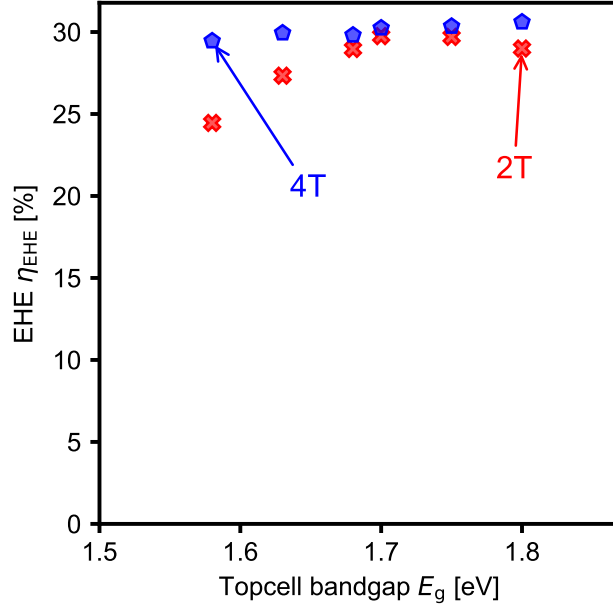


Figure 6: Annual EHE for a perovskite//silicon tandem cell with varying top cell bandgap and Si bottom cell.

the APE for the spectral binning is that this method is independent of any device parameter assumptions. Compared to other binning techniques, such as machine learning, our method offers a simple and computationally fast alternative.

A comparison of the EHE between a current-matched device with 2T and 4T architecture shows only a 2% penalty for the 2T device. Considering additional resistive losses of  $1.87 \Omega \text{ cm}^2$  or optical losses of 5% due to a necessary TCO layer for the module integration of a 4T device results in parity for both architectures in terms of energy yield. A first calculation with our in-house TCO indicates that this can be a realistic assumption for the required TCO layer. A detailed investigation of the optical and electrical properties of the TCO layer on various tandem architectures is planned for future work.

The variation of the top cell bandgap shows that it is essential to have a current-matched device to achieve similar EHE for 2T and 4T devices. A device that is not current-matched, e.g., with a bandgap of 1.58 eV, results in a 17%<sub>rel</sub> lower EHE for the 2T device compared to the 4T device. In a future study, we plan to investigate whether this is also true for other sites, which may show a higher deviation of the spectra from the AM1.5G spectrum.

### Acknowledgements

This work was authored by the National Renewable Energy Laboratory, operated by Alliance for Sustainable Energy, LLC, for the U.S. Department of Energy (DOE) under Contract No. DE-AC36-08GO28308. Funding was provided by the U.S. Department of Energy’s Office of Energy Efficiency and Renewable Energy (EERE) under the Solar Energy Technologies Office Award Number 38266. This report was prepared as an account of work sponsored by an agency of the United States Government. Neither the United States Government nor any agency thereof, nor any of their employees, makes any warranty, express or implied, or assumes any legal liability or responsibility for the accuracy, completeness, or usefulness of any information, apparatus, product, or process disclosed, or represents that its use would not infringe privately owned rights. Reference herein to any specific commercial product, process, or service by trade name, trademark, manufacturer, or otherwise does not necessarily constitute or imply its endorsement, recommendation, or favoring by the United States Government or any agency thereof. The views and opinions of authors expressed herein do not necessarily state or reflect those of the United States Government or any agency thereof. We would also like to thank the Institute for Solar Energy Research in Hamelin (ISFH) for providing the POLO IBC cells.

## References

- [1] W. E. McMahon, J. F. Geisz, J. Buencuerpo, and E. L. Warren, “A framework for comparing the energy production of photovoltaic modules using 2-, 3-, and 4-terminal tandem cells,” *Sustainable Energy & Fuels*, p. 10.1039.D2SE01167K, 2023.
- [2] F. Gota, M. Langenhorst, R. Schmagel, J. Lehr, and U. W. Paetzold, “Energy Yield Advantages of Three-Terminal Perovskite-Silicon Tandem Photovoltaics,” *Joule*, vol. 4, pp. 2387–2403, Nov. 2020.

- [3] I. Garcia, W. E. McMahon, A. Habte, J. F. Geisz, M. A. Steiner, M. Sengupta, and D. J. Friedman, “Spectral binning for energy production calculations and multijunction solar cell design,” *Progress in Photovoltaics: Research and Applications*, vol. 26, no. 1, pp. 48–54, 2018.
- [4] E. Aydin, T. G. Allen, M. De Bastiani, L. Xu, J. Ávila, M. Salvador, E. Van Kerschaver, and S. De Wolf, “Interplay between temperature and bandgap energies on the outdoor performance of perovskite/silicon tandem solar cells,” *Nature Energy*, vol. 5, pp. 851–859, Nov. 2020.
- [5] M. Babics, M. De Bastiani, E. Ugur, L. Xu, H. Bristow, F. Toniolo, W. Raja, A. S. Subbiah, J. Liu, L. V. Torres Merino, E. Aydin, S. Sarwade, T. G. Allen, A. Razzaq, N. Wehbe, M. F. Salvador, and S. De Wolf, “One-year outdoor operation of monolithic perovskite/silicon tandem solar cells,” *Cell Reports Physical Science*, vol. 4, p. 101280, Feb. 2023.
- [6] T. Moot, J. B. Patel, G. McAndrews, E. J. Wolf, D. Morales, I. E. Gould, B. A. Rosales, C. C. Boyd, L. M. Wheeler, P. A. Parilla, S. W. Johnston, L. T. Schelhas, M. D. McGehee, and J. M. Luther, “Temperature Coefficients of Perovskite Photovoltaics for Energy Yield Calculations,” *ACS Energy Letters*, vol. 6, pp. 2038–2047, May 2021.
- [7] M. Babics, H. Bristow, A. R. Pininti, T. G. Allen, and S. De Wolf, “Temperature Coefficients of Perovskite/Silicon Tandem Solar Cells,” *ACS Energy Letters*, pp. 3013–3015, June 2023.
- [8] S. Reynolds and V. Smirnov, “Modelling Performance of Two- And Four-terminal Thin-film Silicon Tandem Solar Cells under Varying Spectral Conditions,” *Energy Procedia*, vol. 84, pp. 251–260, Dec. 2015.
- [9] M. H. Futscher and B. Ehrler, “Efficiency Limit of Perovskite/Si Tandem Solar Cells,” *ACS Energy Letters*, vol. 1, pp. 863–868, Oct. 2016.
- [10] M. Langenhorst, B. Sautter, R. Schmager, J. Lehr, E. Ahlswede, M. Powalla, U. Lemmer, B. S. Richards, and U. W. Paetzold, “Energy yield of all thin-film perovskite/CIGS tandem solar modules,” *Progress in Photovoltaics: Research and Applications*, vol. 27, no. 4, pp. 290–298, 2019.
- [11] D. L. King, W. E. Boyson, and J. A. Kratochvil, “Photovoltaic array performance model,” Tech. Rep. SAND2004-3535, Sandia National Laboratories (SNL), Albuquerque, NM, and Livermore, CA (United States), Aug. 2004.
- [12] J. Geisz, W. E. McMahon, and E. L. Warren, “PVCircuit.” [github.com/nrel/PVCircuit](https://github.com/nrel/PVCircuit), 2022.
- [13] J. Tong, Z. Song, D. H. Kim, X. Chen, C. Chen, A. F. Palmstrom, P. F. Ndione, M. O. Reese, S. P. Dunfield, O. G. Reid, J. Liu, F. Zhang, S. P. Harvey, Z. Li, S. T. Christensen, G. Teeter, D. Zhao, and M. M. Al-Jassim, “Carrier lifetimes of  $>1$  ms in Sn-Pb perovskites enable efficient all-perovskite tandem solar cells,” *Science*, vol. 364, pp. 475–479, 2019.
- [14] D. H. Kim, C. P. Muzzillo, J. Tong, A. F. Palmstrom, B. W. Larson, C. Choi, S. P. Harvey, S. Glynn, J. B. Whitaker, F. Zhang, Z. Li, H. Lu, M. F. van Hest, J. J. Berry, L. M. Mansfield, Y. Huang, Y. Yan, and K. Zhu, “Bimolecular Additives Improve Wide-Band-Gap Perovskites for Efficient Tandem Solar Cells with CIGS,” *Joule*, vol. 3, pp. 1734–1745, July 2019.
- [15] U. Rau, B. Blank, T. C. M. Müller, and T. Kirchartz, “Efficiency Potential of Photovoltaic Materials and Devices Unveiled by Detailed-Balance Analysis,” *Physical Review Applied*, vol. 7, p. 044016, Apr. 2017.
- [16] G. Li, Z. Su, L. Canil, D. Hughes, M. H. Aldamasy, J. Dagar, S. Trofimov, L. Wang, W. Zuo, J. J. Jerónimo-Rendon, M. M. Byranvand, C. Wang, R. Zhu, Z. Zhang, F. Yang, G. Nasti, B. Naydenov, W. C. Tsoi, Z. Li, X. Gao, Z. Wang, Y. Jia, E. Unger, M. Saliba, M. Li, and A. Abate, “Highly efficient p-i-n perovskite solar cells that endure temperature variations,” *Science*, vol. 379, pp. 399–403, Jan. 2023.
- [17] J. F. Geisz, M. A. Steiner, I. Garcia, R. M. France, W. E. McMahon, C. R. Osterwald, and D. J. Friedman, “Generalized Optoelectronic Model of Series-Connected Multijunction Solar Cells,” *IEEE Journal of Photovoltaics*, vol. 5, pp. 1827–1839, Nov. 2015.
- [18] J. F. Geisz, W. E. McMahon, J. Buencuerpo, M. S. Young, M. Rienäcker, A. C. Tamboli, and E. L. Warren, “Characterization of multiterminal tandem photovoltaic devices and their subcell coupling,” *Cell Reports Physical Science*, vol. 2, p. 100677, Dec. 2021.
- [19] U. Rau and J. H. Werner, “Radiative efficiency limits of solar cells with lateral band-gap fluctuations,” *Applied Physics Letters*, vol. 84, pp. 3735–3737, May 2004.

- [20] T. Stoffel and A. Andreas, “NREL Solar Radiation Research Laboratory (SRRL): Baseline Measurement System (BMS); Golden, Colorado (Data),” 1981.
- [21] R. C. Whitehead, K. T. VanSant, E. L. Warren, J. Buencuerpo, M. Rienäcker, R. Peibst, J. F. Geisz, and A. C. Tamboli, “Optimization of four terminal rear heterojunction GaAs on Si interdigitated back contact tandem solar cells,” *Applied Physics Letters*, vol. 118, p. 6, 2021.
- [22] Q. Emery, M. Remec, G. Paramasivam, S. Janke, J. Dagar, C. Ulbrich, R. Schlatmann, B. Stannowski, E. Unger, and M. Khenkin, “Encapsulation and Outdoor Testing of Perovskite Solar Cells: Comparing Industrially Relevant Process with a Simplified Lab Procedure,” *ACS Applied Materials & Interfaces*, vol. 14, pp. 5159–5167, Feb. 2022.
- [23] T. J. Silverman, M. G. Deceglie, I. R. Repins, T. Zhu, Z. Song, M. J. Heben, Y. Yan, C. Fei, J. Huang, and L. T. Schelhas, “Brief: Daily Performance Changes in Metal Halide Perovskite PV Modules,” *IEEE Journal of Photovoltaics*, pp. 1–3, 2023.
- [24] M. Springer, R. Witteck, T. J. Silverman, J. F. Geisz, W. E. McMahon, and E. L. Warren, “Performance modelling and yearlong outdoor degradation analysis of a gaas//si tandem module,” 2023. to be published.
- [25] C. N. Jardine, T. R. Betts, R. Gottschalg, D. G. Infield, and K. Lane, “Influence of Spectral Effects on the Performance of Multijunction Amorphous Silicon Cells,” in *Photovoltaic in Europe Conference*, pp. 1756–1759., 2002.
- [26] J. M. Ripalda, D. Chemisana, J. M. Llorens, and I. García, “Location-Specific Spectral and Thermal Effects in Tracking and Fixed Tilt Photovoltaic Systems,” *iScience*, vol. 23, p. 101634, Oct. 2020.
- [27] M. W. Wanlass, “A Rigorous Analysis of Series-Connected, Multi-Bandgap, Tandem Thermophotovoltaic (TPV) Energy Converters,” in *AIP Conference Proceedings*, vol. 738, (Freiburg (Germany)), pp. 462–470, AIP, 2004.
- [28] W. E. McMahon, K. E. Emery, D. J. Friedman, L. Ottoson, M. S. Young, J. S. Ward, C. M. Kramer, A. Duda, and S. Kurtz, “Fill factor as a probe of current-matching for GaInP<sub>2</sub>/GaAs tandem cells in a concentrator system during outdoor operation,” *Progress in Photovoltaics: Research and Applications*, vol. 16, no. 3, pp. 213–224, 2008.
- [29] Y. Blom, M. R. Vogt, C. M. Ruiz Tobon, R. Santbergen, M. Zeman, and O. Isabella, “Energy Loss Analysis of Two-Terminal Tandem PV Systems under Realistic Operating Conditions - Revealing the Importance of Fill Factor Gains,” *Solar RRL*, p. 2200579, Feb. 2023.
- [30] M. D. Bastiani, A. S. Subbiah, E. Aydin, F. H. Isikgor, T. G. Allen, and S. D. Wolf, “Recombination junctions for efficient monolithic perovskite-based tandem solar cells: Physical principles, properties, processing and prospects,” *Materials Horizons*, vol. 7, no. 11, pp. 2791–2809, 2020.
- [31] M. Zhang and Z. Lin, “Efficient interconnecting layers in monolithic all-perovskite tandem solar cells,” *Energy & Environmental Science*, May 2022.
- [32] A. M. Ganose, D. O. Scanlon, A. Walsh, and R. L. Z. Hoyer, “The defect challenge of wide-bandgap semiconductors for photovoltaics and beyond,” *Nature Communications*, vol. 13, p. 4715, Aug. 2022.
- [33] G. Yang, Z. Ni, Z. J. Yu, B. W. Larson, Z. Yu, B. Chen, A. Alasfour, X. Xiao, J. M. Luther, Z. C. Holman, and J. Huang, “Defect engineering in wide-bandgap perovskites for efficient perovskite-silicon tandem solar cells,” *Nature Photonics*, July 2022.
- [34] H. Lai, J. Luo, Y. Zwirner, S. Olthof, A. Wiecek, F. Ye, Q. Jeangros, X. Yin, F. Akhundova, T. Ma, R. He, R. K. Kothandaraman, X. Chin, E. Gilshtein, A. Müller, C. Wang, J. Thiesbrummel, S. Siol, J. M. Prieto, T. Unold, M. Stolterfoht, C. Chen, A. N. Tiwari, D. Zhao, and F. Fu, “High-Performance Flexible All-Perovskite Tandem Solar Cells with Reduced Voc-Deficit in Wide-Bandgap Subcell,” *Advanced Energy Materials*, vol. 12, no. 45, p. 2202438, 2022.